Generalized Predictive Current Control (GPCC) for Grid-Tie Three-Phase Inverters

M.G. Judewicz, *Student Member, IEEE,* S.A. González, *Member, IEEE,* N.I. Echeverría, J.R. Fischer, *Member, IEEE,* D.O. Carrica, *Member, IEEE*

***Abstract*—This work proposes a linear Generalized Predictive Current Control (GPCC) for Grid-Connected Voltage Source Inverters, which presents a fast response to current reference step changes, parameter variation robustness and low distortion at the output currents, with reduced computational effort. Experimental results on a $10\,\mathrm{kW}$ converter connected to a real grid are shown and the proposed controller is compared against a classical proportional resonant (PR) controller.**

***Index Terms*—Generalized Predictive Control, Digital current controller, Grid-Tie Voltage-Source Inverters, Renewable Energy Systems.**

I. INTRODUCTION

In a Distributed Power Generation System (DPGS) scheme, Grid-Connected Current-Controlled Voltage Source Inverters (CC-VSI) are the main power converter topology used in the interconnection of distributed energy resources to the grid [1]. Its main goal is to inject current into the electrical power grid amidst several disturbances that affect the system, which come from the grid, e.g. grid voltage fluctuations, total harmonic distortion (THD_v), voltage sags, or the inverter nonlinearities, such as load inductance variations or converter dead-times. In particular, when high switching frequency is used to reduce the size and cost of reactive components throughout the system, dead-time effects become an important issue in grid-tied applications which produce distortions rich in harmonics not easily mitigated by standard control techniques [2]. Therefore, current quality standards such as IEEE Std. 1547-2003 or the IEC-61000-3-2, have been proposed in order to set a limit on the grid current total harmonic distortion (THD_i). Undesirable harmonic content disrupts power transformer operation, produces excessive power dissipation in the transmission lines, and disturbs neighboring loads. Therefore, optimal current control performance is of uttermost importance in the design of Grid-Connected VSIs. Current control key requirements are: fast reference tracking for accurate active and reactive power tracking, high closed-loop bandwidth in order to reject disturbances, and robustness against system model mismatch.

Manuscript received December 29, 2014; revised April 14, 2015, May 19, 2015 and September 23, 2015; accepted November 3, 2015.

The authors are with the ICYTE (Instituto de Investigaciones Científicas y Tecnológicas en Electrónica), Facultad de Ingeniería, Universidad Nacional de Mar del Plata and CONICET (Consejo Nacional de Investigaciones Científicas y Técnicas).

Current control in VSIs can be classified in two main categories. The first group comprises nonlinear control methods such as Hysteresis Based (HCC) [3], Sliding Mode (SMC) [4] and Finite-Control-Set Model Predictive Control (FCS-MPC) [5]–[10]. These controllers track the reference by directly driving the inverter switches. These strategies have the disadvantage of variable switching frequency, which generates a spread spectrum even at low frequencies, difficult to filter, leading to higher THD_i values. The situation can improve by increasing switching frequency and/or output inductance. Nevertheless, this actions also increase power dissipation and converter cost. In the case of FCS-MPC, some additional measures can be taken in order to reduce current spectrum spreading by including a digital filter on the cost function [11], [12] or by calculating the optimal switching times acting as an incorporated modulator [13]. Another nonlinear approach is Neuro-Fuzzy Control (NFC) [14], which takes advantage of both designer knowledge of the system and a trained neural network. Nevertheless, its design is an iterative process and heuristical in nature. Therefore, optimum controller performance might be difficult to achieve.

The second group comprises linear controllers such as PI-based synchronous reference frame [15], state feedback [16], proportional resonant (PR) [17] and pole placement techniques [18], which make use of a Pulse Width Modulator (PWM) keeping a constant switching frequency, while following the reference by applying a duty cycle on the switches. Their design is based on a linear model of the system in order to guarantee closed-loop system stability in the frequency domain obtaining a conservative and unlikely optimal result. Also, in the particular case of the standard PR controllers, their design requires a tradeoff between steady-state error and robustness, and they are also sensitive to grid frequency variations. On the other hand, linear model predictive control (MPC) strategies make use of the system model in order to obtain an optimal control formulation based on some optimality criteria, along a prediction horizon [19]. Current tracking error dynamics is generally the main optimization objective, as is the case of classic deadbeat predictive control [20], which presents a fixed time-optimal prediction and control horizon strategy. Unfortunately, deadbeat strategies are sensitive to parameter variations. In [21], the authors extend its robustness by including a Luenberger observer and an expanded model with calculation delays.

Another linear predictive control strategy is Receding Horizon Control (RHC) [22], which is a type of MPC with prediction and control horizon lengths as design parameters. In

[23], an explicit RHC strategy is used, which defines a look-up table (LUT) for different operating points of the system, based on model constraints. This formulation is useful only when considerable amount of physical system constraints exist. In the unconstrained case, a more computationally efficient RHC strategy can be used, which gives a fixed-coefficients transfer function, without losing performance. One such formulation can be devised using Generalized Predictive Control (GPC) [24], [25], which is based on a transfer function model of both the plant and the disturbances. The disturbance model acts like the inclusion of an observer, which improves control loop disturbance rejection. Also, it uses a quadratic cost function that includes an input variation term which affects control dynamics. This type of MPC strategy has been scarcely used in the control of power converters [26]–[30], motivating its evaluation for grid-tied applications. In [26], GPC is used to control the stator current of an induction motor, encouraging the experimental validation of the proposal. Later, in [27] an experimental evaluation of GPC is done for the control of a single phase PWM inverter used as a power supply, obtaining good results. [28] introduces the GPC for field oriented control of induction machines and [29] simulates the GPC as a power flow controller on a UPFC. Finally, [30] applies GPC to a UPS application using the Diophantine equation formulation. Nevertheless, none of these works develops an explicit design strategy, which is necessary in order to use this controller in industrial power converters, and is therefore introduced in this work.

For the first time, a complete design procedure and experimental validation of GPC on a grid-tied three-phase two-level inverter for distributed power generation systems (DPGS) is presented. The inclusion of a disturbance transfer function and its relationship with the observer stability and dynamics is explored. Also, an analysis of cost function parameter selection for bandwidth and robustness criteria is made, by which a novel *a priori* design method for this controller is introduced.

The work is organized as follows: in section II, a mathematical description of the system model is obtained; in section III, the theory behind GPC is exposed; in section IV, a novel GPC controller design criteria is introduced; in section V, the proposed controller practical implementation is presented, and in section VI, experimental results are obtained for both steady-state and transient responses and contrasted with those obtained through the use of a PR-based controller. The obtained results, in terms of output current THD and robustness against parameter mismatch are compared for both techniques. Also, controller calculation time is measured and a performance comparison is made with both predictive and standard control techniques. Finally, section VII presents the conclusions obtained in this work.

II. System Model

The system can be represented as shown in Fig. 1, which will be used for the controller design process and simulations. Power generated from the renewable source is modeled as current i_{DC} that charges the dc-link. Each capacitor is charged

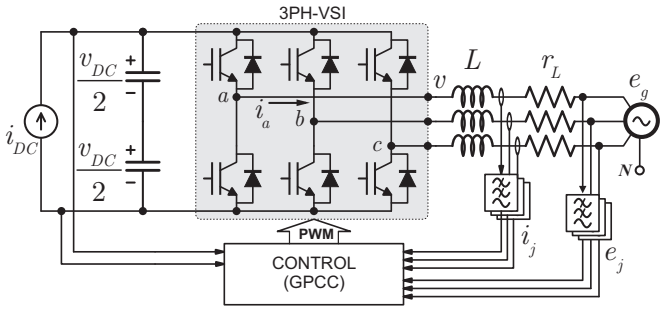

Fig. 1. Grid-Connected Voltage Source Inverter in a 3W configuration.

to voltage $v_{DC}/2$. Current i_j, with $j = \{a, b, c\}$ is injected to the grid by means of an inductor filter L with an associated parasitic resistance represented by r_L. e_j represents grid voltage in the abc reference frame.

As the system is connected in a three-phase three-wire (3W) configuration, the controller has two degrees of freedom, i.e., two of the three phase currents can be independently controlled [31]. This type of connection brings a higher filtering capability than its four wire (4W) counterpart, with the same inductance per phase. If the load is balanced, then,

$$Z_{eq} = 1.5Z, \tag{1}$$

where $Z = r_L + sL$ and $Z_{eq} = R_{eq} + sL_{eq}$. R_{eq} and L_{eq} are the equivalent parasitic resistance and filter inductance respectively of the 3W load-configuration connection which results in the equivalent impedance Z_{eq}. In this work, a separate controller is applied to phases a and b independently, being c the dependent current phase.

Using the previous assumptions, the per-phase model can be described by the following equation

$$v_j(t) = R_{eq} i_j(t) + L_{eq} \frac{di_j(t)}{dt} + e_j(t), \tag{2}$$

where $v_j(t) = \frac{v_{DC}}{2}(2d_j(t) - 1)$ is the voltage applied to the load by the inverter and $d_j(t)$ is the duty cycle of leg j. In practice, the controller gives a desired voltage input to the load and then the duty cycle is calculated as

$$d_j(t) = \frac{1}{2}\left(\frac{2v_j(t)}{v_{DC}} + 1\right), \tag{3}$$

where $0 \leq d_j(t) \leq 1$. Using (2), a transfer function between applied voltage and output current in the continuous domain can be obtained for each phase

$$G_j(s) = \frac{1}{R_{eq} + sL_{eq}}. \tag{4}$$

By means of a ZOH circuit, the output current is sampled with a sampling period, T_s, chosen in order to guarantee $R_{eq}T_s/L_{eq} \ll 1$. Thus a discrete transfer function is obtained,

$$G_{jd}(z^{-1}) = \frac{m_1 z^{-1}}{1 - n_1 z^{-1}}. \tag{5}$$

Generally, non-modelled control system delays reduce overall stability. A simple way to overcome this problem is to include an additional unit delay to (5), such that,

$$G_{jd}(z^{-1}) = \frac{m_1 z^{-2}}{1 - n_1 z^{-1}}. \tag{6}$$

This is a conservative model for delays much shorter than the sampling period. Advanced system models include a more accurate representation of calculation delays [21]. Nevertheless, as will be shown in IV, with a proper design, GPC is able to deal with model mismatch, removing the need of complex models and reducing calculation times.

III. GPC Design

The design process of GPC includes system model description and cost function configuration steps. The model is used to predict the controlled variable trajectory over the chosen horizon and the cost function is used to determine the optimal control input in accordance with the chosen optimality terms. In the following sections both design steps are described and control law transfer function coefficients can be obtained in this way.

A. Model

In order to design a GPC control loop, the model must be expressed as a transfer function formulation of the form,

$$A(z^{-1})\Delta y(k) = z^{-d}B(z^{-1})\Delta w(k) + C(z^{-1})\nu(k), \quad (7)$$

where $y(k)$ is the controlled variable, $w(k)$ is the controlled plant input, $\nu(k)$ is an unmeasurable disturbance signal, $\Delta = 1 - z^{-1}$ is the discrete differentiation operator,

$$A(z^{-1}) = 1 - a_1 z^{-1} - ... - a_n z^{-n} \quad (8)$$

$$B(z^{-1}) = b_1 z^{-1} + ... + b_p z^{-p} \quad (9)$$

$$C(z^{-1}) = z^{-1} + c_2 z^{-2} + ... + c_q z^{-q} \quad (10)$$

are the system model polynomials in the discrete time domain and d is the number of additional discrete delays of the model, not included in $B(z^{-1})$. $A(z^{-1})$ and $B(z^{-1})$ are obtained from the plant transfer function (6), so $B(z^{-1}) = m_1 z^{-1}$ and $A(z^{-1}) = 1 - n_1 z^{-1}$, and $d = 1$. The polynomial $C(z^{-1})$ acts as an observer and its coefficients are chosen so as to place its roots inside the unit circle, guaranteeing observer stability. Therefore, by including this term in the transfer function model of the plant, observer design is very much simplified. In [30], $C(z^{-1})$ is chosen to be unity. Nevertheless, based on [32], a polynomial of the form $C(z^{-1}) = z^{-1} + c_2 z^{-2}$, with $c_2 = -0.8$, is an optimal tradeoff between estimation speed of convergence and noise filtering.

B. Cost function

The cost function of a GPC problem is defined as the sum of quadratic terms,

$$V(k) = \sum_{i=H_w}^{H_p} Q(i)\left[\hat{y}(k+i|k) - r(k+i)\right]^2 + \sum_{i=0}^{H_c-1} R(i)\left[\Delta\hat{w}(k+i|k)\right]^2, \quad (11)$$

where:

$\hat{y}$	Predicted output
r	Reference trajectory
$\Delta\hat{w}$	Control increment
H_w	Prediction horizon window offset
H_p	Prediction horizon length
H_c	Control horizon length
$Q(i)$	Error weighting sequence
$R(i)$	Control increment weighting sequence

and the argument $(k+i|k)$ means that the prediction of the variable at time $k+i$ is calculated at time k.

The first term of the cost function evaluates output trajectory error with respect to the reference and the second term weighs the magnitude of the change in the control input. Both terms affect total cost differently in accordance with the selection of $Q(i)$ and $R(i)$. If normalized weighting sequences are used then $Q(i) = 1$ for all i, and $R(i) = \lambda_i$. If a constant value of R is chosen, i.e. $R(i) = \lambda$, the entire control sequence is weighed equally at every time instant, simplifying the controller design process. Nevertheless, its value affects controller performance, thus its proper selection is important, as will be discussed in section IV.

C. GPC formulation

Based on the previous subsections a state space representation of the Generalized Predictive Controller can be obtained [33]. First, the state vector is built as

$$x(k) = [y(k), y(k-1), w(k-1), \nu(k-1)]^T, \quad (12)$$

which is estimated by means of an observer described by

$$\hat{x}(k|k) = \hat{x}(k|k-1) + L'[y(k) - \hat{y}(k|k-1)] \quad (13)$$

$$\hat{x}(k+1|k) = \mathcal{A}\hat{x}(k|k) + \mathcal{B}w(k) \quad (14)$$

$$\hat{y}(k|k-1) = \mathcal{C}\hat{x}(k|k-1). \quad (15)$$

This observer is used in order to determine $\nu(k-1)$ only, because the remaining state variables values can be obtained by direct measurement.

The state space model matrices are described as

$$\mathcal{A} = \begin{bmatrix} \mathcal{A}_{11} & \mathcal{A}_{12} & \mathcal{A}_{13} \\ 0 & \mathcal{A}_{22} & 0 \\ 0 & 0 & \mathcal{A}_{33} \end{bmatrix} \quad (16)$$

$$\mathcal{B} = [m_1, 0, 1, 0]^T \quad (17)$$

$$\mathcal{C} = [1, 0, 0, 0], \quad (18)$$

where

$$\mathcal{A}_{11} = \begin{bmatrix} 1+n_1 & -n_1 \\ 1 & 0 \end{bmatrix} \quad (19)$$

$$\mathcal{A}_{12} = \begin{bmatrix} -m_1 \\ 0 \end{bmatrix} \quad (20)$$

$$\mathcal{A}_{13} = \begin{bmatrix} c_2 \\ 0 \end{bmatrix} \quad (21)$$

$$\mathcal{A}_{22} = \begin{bmatrix} 0 & 0 \end{bmatrix} \quad (22)$$

$$\mathcal{A}_{33} = \begin{bmatrix} 0 & 0 \end{bmatrix}. \quad (23)$$

The observer gain is defined as

$$L' = [1, 0, 0, 1]^T, \tag{24}$$

which, in combination with c_2, gives a stable observer such that

$$max(|eig(\mathcal{A}(I - L'\mathcal{C}))|) < 1. \tag{25}$$

With this equivalent state space representation, the error over H_p can be described by

$$\mathcal{E}(k) = T(k) - \Psi\hat{x}(k|k) - \Upsilon w(k-1), \tag{26}$$

where $T(k) = [r(k)...r(k+H_p)]^T$ is the sequence of reference values up to time $k + H_p$ and

$$\Psi = \underbrace{\begin{bmatrix} \mathcal{C} & 0 & ... & 0 \\ 0 & \mathcal{C} & ... & 0 \\ \vdots & \vdots & \ddots & \vdots \\ 0 & 0 & ... & \mathcal{C} \end{bmatrix}}_{H_p \text{ rows}} \begin{bmatrix} \mathcal{A} \\ \vdots \\ \mathcal{A}^{H_p} \end{bmatrix} \tag{27}$$

$$\Upsilon = \begin{bmatrix} \mathcal{C} & 0 & ... & 0 \\ 0 & \mathcal{C} & ... & 0 \\ \vdots & \vdots & \ddots & \vdots \\ 0 & 0 & ... & \mathcal{C} \end{bmatrix} \begin{bmatrix} \mathcal{B} \\ \vdots \\ \sum_{i=0}^{H_p-1} \mathcal{A}^i\mathcal{B} \end{bmatrix}. \tag{28}$$

The second and third terms in the right hand side of the error equation represent the effect of the present estimated state and of the previous control input in both the present and future output samples of the plant, respectively.

The optimal control input can be obtained by multiplying $\mathcal{E}(k)$ with an optimal gain vector K_{GPC} which can be calculated as

$$K_{GPC} = [1, 0, ..., 0]\mathcal{H}^{-1}\Theta^T Q, \tag{29}$$

where

$$\Theta = \begin{bmatrix} \mathcal{B} & 0 & ... & 0 \\ \mathcal{A}\mathcal{B} + \mathcal{B} & \mathcal{B} & ... & 0 \\ \vdots & \vdots & \ddots & \vdots \\ \sum_{i=0}^{H_p-1} \mathcal{A}^i\mathcal{B} & ... & ... & \sum_{i=0}^{H_p-H_c} \mathcal{A}^i\mathcal{B} \end{bmatrix} \tag{30}$$

$$\mathcal{H} = \Theta^T Q\Theta + R. \tag{31}$$

Then,

$$\Delta w_{opt}(k) = K_{GPC}\mathcal{E}(k) \tag{32}$$

and

$$w(k) = w(k-1) + \Delta w_{opt}(k). \tag{33}$$

As seen in (29), K_{GPC} depends on the H_p, H_c and λ (indirectly through R matrix) controller design parameters, as they were presented in the previous section as part of the GPC cost function formulation. As mentioned before, there is an upper bound on both lengths for which higher values do not give appreciable improvement on the controller performance. In the case of the controller for this plant, a prediction horizon of $H_p = 8$, and a control horizon of $H_c = 6$, are the minimum values for which longer lengths give infinitesimal improvements, and are therefore chosen for the calculations. Also, $H_w = d + 1 = 2$, which includes both the inherent discretization delay and the calculation time delay of the model obtained in section II. In the case of λ, its selection will be explained in the following section, which leads to a transfer function $G_{GPC}(z^{-1})$ controller representation.

IV. λ PARAMETER SELECTION CRITERIA

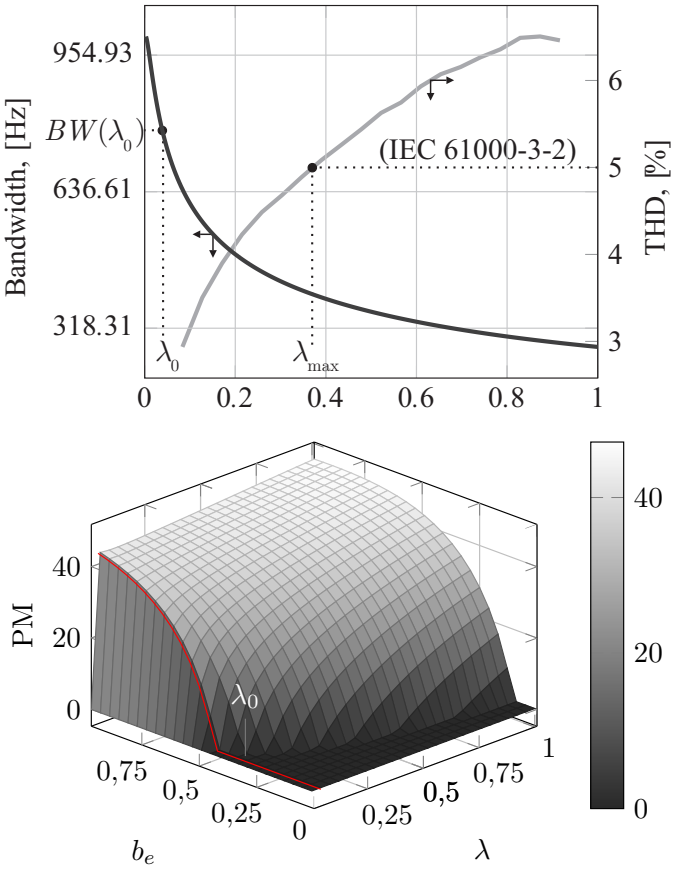

Fig. 2. Controller bandwidth (BW) as a function of λ (above), under null parameter mismatch, and control system phase margin (PM) as a function of λ and b_e (below), for $0 \leq \lambda \leq 1$. A chosen value of λ_0 is highlighted.

As shown in (31), controller design depends on the selection of the R matrix which depends on the λ parameter. Generally, the selection of weighting parameters in MPC is an iterative *a posteriori* process, i.e. the designer makes a "tuning" procedure until the results reflect the desired performance. In this work, an *a priori* selection is made based on controller bandwidth and robustness criteria, eliminating the need of an iterative solution, as explained next.

Controller bandwidth is defined as the cutoff frequency of the open loop transfer function $G_{OL}(z^{-1})$ of the controlled plant, which depends on the GPC transfer function in the form of

$$G_{OL}(z^{-1})|_\lambda = G_{GPC}(z^{-1})|_\lambda \cdot G_{jd}(z^{-1}) \tag{34}$$

where $G_{GPC}(z^{-1})|_\lambda$ reflects the controller dependence on the selection of the λ parameter, assuming both horizon lengths H_p and H_c previously selected. For example, using values given in table I for $\lambda = 0$,

$$G_{GPC}(z^{-1})|_{\lambda=0} = \frac{34.16 - 28.96z^{-1}}{1 + 0.1593z^{-1} - 1.159z^{-2}}, \tag{35}$$

This article has been accepted for publication in a future issue of this journal, but has not been fully edited. Content may change prior to final publication. Citation information: DOI 10.1109/TIE.2015.2508934, IEEE Transactions on Industrial Electronics

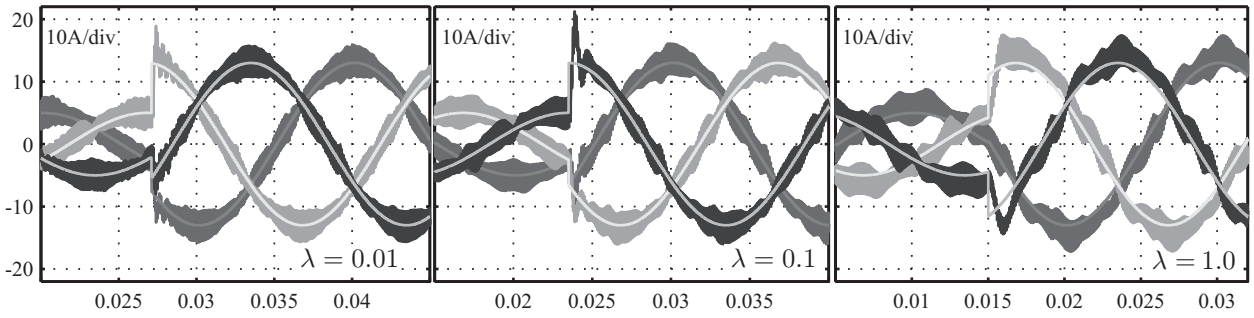

Fig. 3. Simulation results showing the output current behavior for different values of λ. In all cases, a step from $5\,\mathrm{A_p}$ to $13\,\mathrm{A_p}$ in the output current reference is made in arbitrary time instants.

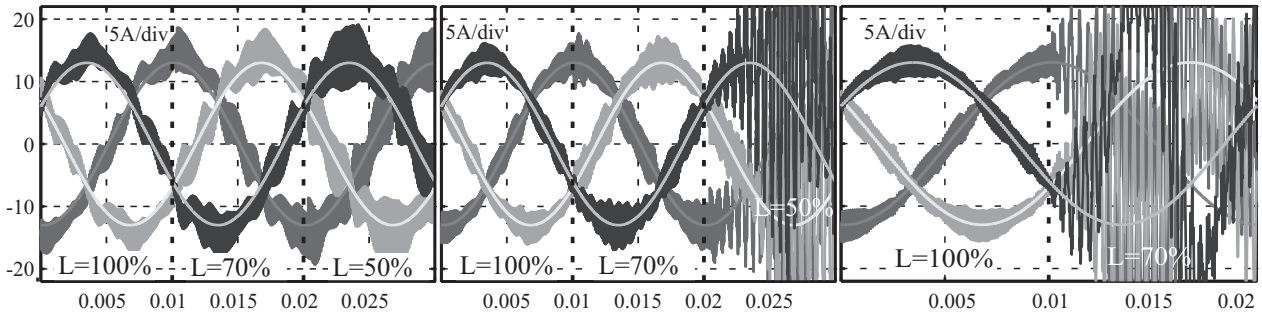

Fig. 4. Simulation results showing the controlled output current waveforms under different parameter mismatch situations, dynamically varying load inductance L, for different values of λ. From left to right, $\lambda = 1, 0.1, 0.01$.

and for $\lambda = 0.1$,

$$G_{GPC}(z^{-1})|_{\lambda=0.1} = \frac{9.846 - 8.544z^{-1}}{1 - 0.9967z^{-1} - 0.003257z^{-2}}, \quad (36)$$

where for each case a different $G_{OL}(z^{-1})$ and thus different bandwidths are obtained. Therefore, setting a given interval for the λ values, a relationship between λ and controller bandwidth can be obtained. A chosen interval of $0 \leq \lambda \leq 1$ results in the upper graphic of Fig. 2. It can be seen that controller bandwidth falls abruptly for $0 \leq \lambda \leq 0.1$, and then it continues descending in a more gradual manner. Ultimately, with increasing values of λ, a reduction of controller bandwidth is expected. In the same graphic, a plot of THD_i for the same interval is also shown, which was obtained using a circuit simulation tool, including inverter dead-time $T_d = 2.5\,\mu\mathrm{s}$ and calculation delay $t_d = 100\,\mu\mathrm{s}$ in order to reflect real life situations. The THD_i value was obtained using an embedded THD calculator available in the circuit simulator software. This plot shows that, in order to meet the maximum THD_i limits, i.e. below 5%, λ must be less than 0.4, approximately, which introduces an upper bound on λ for its practical use. Small bandwidth not also produces undesirable effects on THD_i but also on the transient response, as can be seen in Fig. 3, where a simulation of a step in the output current amplitude is shown for $\lambda = 0.01$, $\lambda = 0.1$ and $\lambda = 1.0$, which are different orders of magnitude away of each other. As seen in the simulation results, the higher the value of λ, the worse the performance of the controller in terms of transient response.

On the other hand, a good measure of a control system robustness is the phase margin under plant model mismatch. Phase margin is the distance, in sexagesimal degrees, to the $-180°$ phase value at the cutoff frequency of $G_{OL}(z^{-1})$. In this case,

$$G_{OL}(z^{-1})|_{\lambda,b_e} = G_{GPC}(z^{-1})|_{\lambda} \cdot G_{jd}(z^{-1})|_{b_e} \quad (37)$$

where $G_{jd}(z^{-1})|_{b_e}$ reflects the model transfer function dependence with certain parameter variation b_e. In this particular case, $b_e = L_{real}/L_{model}$, as the inductance variation has the most detrimental effect on controller stability. Therefore, a relationship of λ and b_e with phase margin can also be obtained, as shown in the lower graphic of Fig. 2. It is seen that lower values of λ have greater sensitivity to b_e variations, and have larger regions of instability, i.e. where there is null phase margin. Therefore, robustness requirements impose a lower bound on λ, as can be seen in Fig. 4. Simulation results show that for $\lambda = 0.01$, an inductance reduction of 30% leads the system to instability. For $\lambda = 0.1$, this reduction can be tolerated but a 50% decrease becomes the robustness limit for this situation. Finally, for $\lambda = 1$, even a 50% inductance reduction can be tolerated but current quality is severely degraded.

The previous analysis shows that the selection of λ must be a trade-off between bandwidth (BW) and robustness, which depends on the specific application in which the GPC controller will be used. In this work, a suitable selection is made at $\lambda_0 = 0.04$, as it gives a $PM > 30°$ @ $b_e = 0.7$ and $BW = 779\,\mathrm{Hz}$ which is more than a decade above the fundamental frequency of the reference $f_r = 50\,\mathrm{Hz}$.

Once the parameters are chosen, the K_{GPC} vector is fixed and an equivalent transfer function representation can be obtained. Then, its associated difference equation is used

in a digital processor, making the controller implementation straightforward.

V. Control System Implementation

A complete scheme of the control system is shown in Fig. 5. Injected current is measured with current sensors in phases a and b. As was previously mentioned, the third current is not directly controlled, meaning that a third sensor is not necessary. Each of the sensed currents is filtered with an antialiasing LPF, with $f_c = 10\,\text{kHz}$, which is below the Nyquist frequency of the sampling frequency $f_s = 30\,\text{kHz}$.

An additional digital decimation moving average FIR filter of the form

$$\bar{i}_j(k) = \frac{1}{3}(i_j(k-1) + i(k) + i(k+1)) \tag{38}$$

is used. As this filter is non-causal, a modification of its formulation needs to be done. Its causality can be achieved by delaying each filter term by one sample, at the expense of a considerable rise on phase rotation. Alternatively, $i_j(k+1)$ can be replaced by an estimation based on previous samples. By the following interpolation,

$$\begin{aligned}\hat{\bar{i}}_j(k) &= \bar{i}_j(k-1) + (\bar{i}_j(k-1) - \bar{i}_j(k-2)) \\ &= 2\bar{i}_j(k-1) - \bar{i}_j(k-2)\end{aligned} \tag{39}$$

a filter output estimation at time k is obtained. Delaying (38) by one and two samples and replacing at (39),

$$\hat{\bar{i}}_j(k) = \frac{2}{3} + \frac{1}{3}i_j(k-1) + \frac{1}{3}i_j(k-2) - \frac{1}{3}i_j(k-3) \tag{40}$$

is obtained. Then, applying z transform,

$$H_{FIR}(z^{-1}) = \frac{2}{3} + \frac{1}{3}z^{-1} + \frac{1}{3}z^{-2} - \frac{1}{3}z^{-3} \tag{41}$$

is obtained. This is used to bring the samples to the switching frequency of the VSI, which is $f_{sw} = 10\,\text{kHz}$. The reason for this configuration is that the phase shift of the analog antialiasing filter can be reduced at the cutoff frequency of the control loop, placing its poles at higher frequency and improving its overall stability.

Phase voltages are measured in each phase and also filtered with an antialiasing filter with $f_c = 4\,\text{kHz}$, as it is sampled at $f_s = 10\,\text{kHz}$. These measurements are used by the VSPF-PLL [34], in order to generate references relative to the phase of the voltage waveform. This type of PLL was chosen to guarantee power injection even under grid unbalances. The reference signals $r_a(k)$ and $r_b(k)$ are built as

$$r_j(k) = A(k)sin(p_j(k) + \phi(k)), \tag{42}$$

with $j = \{a, b\}$. $A(k)$ is the amplitude of the sinusoidal reference signal, and $\phi(k)$ is the phase offset of the reference relative to the voltage waveform phase. They are used as control system inputs in order to change active and reactive power injection to the grid.

The GPC controller is implemented as a discrete transfer function in the form of a difference equation which uses the error between the reference and output current samples and gives the control algorithm output sample $w_j(k)$, $j = \{a, b\}$ as a result. By means of the method explained in section III, and the chosen values of H_p, H_c and λ, the resulting transfer function is

$$G_{GPC} = \frac{w_j(k)}{\varepsilon_j(k)} = \frac{17.58 - 15.07z^{-1}}{1 - 0.5881z^{-1} - 0.4119z^{-2}}. \tag{43}$$

where $\varepsilon_j(k) = r_j(k) - i_j(k)$. The control algorithm output for the uncontrolled phase is

$$w_c(k) = -w_a(k) - w_b(k). \tag{44}$$

To each of these outputs, a grid voltage feedforward term is added in order to reject its disturbance effect, and consists of the actual grid voltage sample $e_j(k)$, $j = \{a, b, c\}$. The resulting feedforward compensated control input $u_j(k)$ is fed into the PWM module, with proper gain correction as shown in (3).

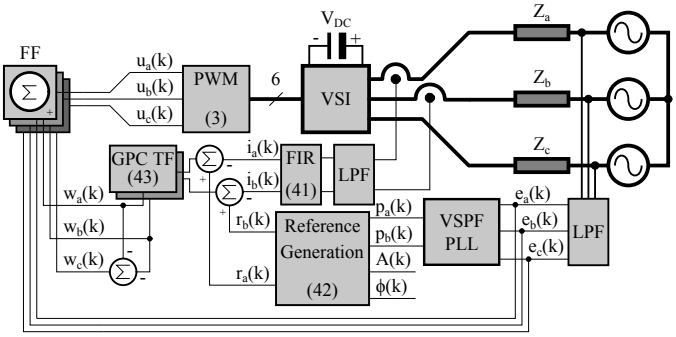

Fig. 5. Proposed control system block diagram. Relevant equations are in parenthesis into the blocks.

A. Hardware setup

Fig. 6 shows the hardware configuration used for experimental results. The VSI was built around Semikron SKM75GB176D 1700V 45A IGBT modules and its DC-Bus was built with two $2200\,\mu\text{F}$ 500V aluminum capacitors. VSI output current is sensed with LEM LA-125P Hall-Effect current transducers, conditioned and later sampled by the microcontroller. The digital control framework chosen is composed of a custom board based on TI TMS320F28335 Floating-point Digital Signal Controller (DSC) which has been widely adopted and used for industrial control. Its 12-bit resolution ADC core with built-in S & H was used to sample all the control variables and its 16-bit Enhanced Digital 3PH-PWM (ePWM) module was used to drive the power stage.

VI. Experimental results

The proposed controller was tested experimentally in order to evaluate its steady-state and dynamic performance in a three-phase three-wire (3W) configuration with independent PWM modulators. Operational conditions for both scenarios are described in table I. Also, it was compared against a standard Proportional Resonant (PR) controller, designed following a systematic method [35]. Nevertheless, some of its parameter selection criteria are given in a certain range and, therefore, the resulting controller is not necessarily optimal. Its design parameters are listed in table II. The proportional gain

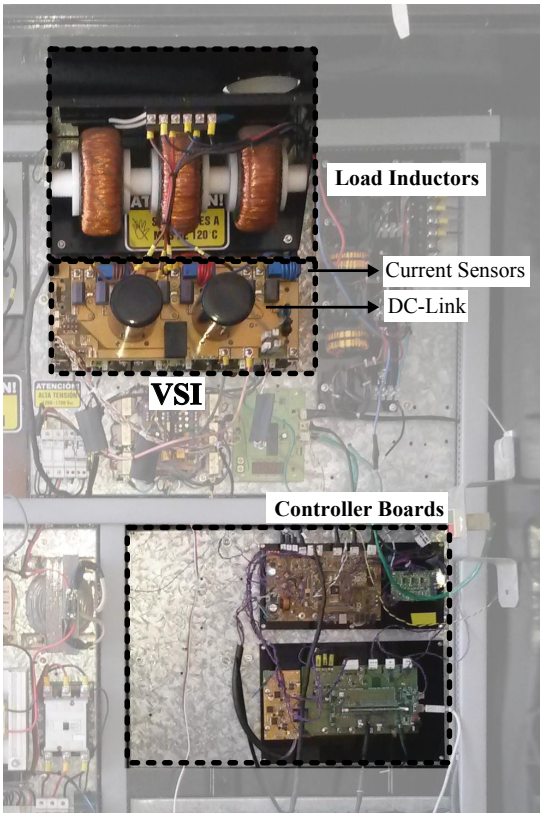

Fig. 6. Photograph highlighting the most relevant parts of the power converter.

K_p is calculated directly and depends on the model inductance L and the chosen cutoff frequency f_c. On the other hand, the resonant gain K_r is chosen as the midpoint between the lower and the upper bounds. This bounds depend on the model and operating conditions, and also on f_c, the output current steady state error η and the desired minimum phase margin ϕ. Choosing the midpoint guarantees the maximum distance from each of the bounds, preventing undesired situations.

TABLE I
NOMINAL OPERATIONAL CONDITIONS.

Nominal output power, P_{nom}	10 kW
Output phase resistance, r_L	0.7 Ω
Output phase inductance, L	1.7 mHy
Grid phase voltage, V_g	220 V_{rms}
Switching frequency (3W), f_s	10 kHz
Programmed dead-time, t_d	2.5 μs
Pole-to-pole dc bus voltage range (3W), $2V_b$	760 V_{min}, 820 V_{max}
Grid coupling at PCC (3W)	direct connection

A. Steady-state performance

In the first set of tests, the steady state performance of the proposed current controller is evaluated and compared with the standard proportional resonant (PR) controller, which are shown in Fig. 8a for the GPCC and Fig. 8b for the PR controller. A THD_i of 2.7% is achieved with GPCC outperforming traditional PR control which has a $THD_i = 5.2\%$, even under higher grid distortion. The THD_i of the proposed

TABLE II
PR CONTROLLER DESIGN PARAMETERS.

Cutoff frequency, f_c	800 Hz
Desired output current steady-state error, η	1%
Desired minimum phase margin, ϕ	45°
Resulting proportional gain, K_p	12.8177
Resonant gain lower bound, $K_{r_{min}}$	66.4918
Resonant gain upper bound, $K_{r_{max}}$	5119.9
Selected resonant gain, K_r	2593.2

IEC 61000-3-2 Harmonics, Class A

THD-F	2.71 %
RMS	9.26 A
Overall	Pass
POHC	104mA
POHL	251mA

	Freq (Hz)	Mag (%)	Mag RMS (A)	Limit (A)	Pass Fail	Max all Windows (A)	200 % Limit	POHC Limit
1	49.96	100	9.20	----.	n/a	9.20	n/a	n/a
2	99.93	407m	37.5m	1.08	Pass	39.1m	Pass	n/a
3	149.9	221m	20.3m	2.30	Pass	20.6m	Pass	n/a
4	199.9	93.9m	8.64m	430m	Pass	9.41m	Pass	n/a
5	249.8	1.45	133m	1.14	Pass	134m	Pass	n/a
6	299.8	123m	11.3m	300m	Pass	11.5m	Pass	n/a
7	349.8	980m	90.1m	770m	Pass	91.3m	Pass	n/a
8	399.7	102m	9.39m	230m	Pass	9.90m	Pass	n/a
9	449.7	279m	25.7m	400m	Pass	26.9m	Pass	n/a
10	499.6	49.8m	4.58m	184m	Pass	5.13m	Pass	n/a

Fig. 7. 10.2 kW steady state THD measurement and detailed harmonic content with successful IEC61000-3-2 automatic harmonic compliance test.

controller meets the IEC61000-3-2 standard as shown in Fig. 7. A Tektronix MSO 4034B 350 MHz with a sample time of 0.5 MS/s per phase was used to measure inverter output currents directly. Effective accuracy on both voltage and current was $\pm 0.16\% f.s.$ with 50 A full-scale probes and harmonic analysis up to the 40th component.

B. Transient performance

The capability of rapidly following abrupt changes in the reference is a necessary feature for a controller to meet the demands of grid connected applications. Again, the proposed current controller dynamic response is compared with that of the PR controller. Fig. 9 shows a reference amplitude step change from 5 A_p to 13 A_p while maintaining null reactive power. As can be seen, the proposed strategy has negligible overshoot and oscillations, while the PR controller presents a 30% undesired overshoot and severe oscillations for 6 ms, approximately.

Another key aspect of a grid-tied DPGS is the ability to inject reactive power into the grid. This is due to the fact that DPGSs are required to stay connected to the grid and must inject sinusoidal, symmetrical, reactive power in order to enhance voltage levels during grid faults [36]. In order to verify the effectiveness of GPCC at controlling output power factor, a step change from 0° to 30° with respect to the grid voltage phase, is commanded and compared against the PR response, as seen in Fig. 10. Although both controllers achieve the desired phase shift with respect to grid voltage, in the case of the GPCC the output current shows an almost instant phase-step change, as opposed to the PR which has oscillations with a settling time of 10 ms.

This article has been accepted for publication in a future issue of this journal, but has not been fully edited. Content may change prior to final publication. Citation information: DOI 10.1109/TIE.2015.2508934, IEEE Transactions on Industrial Electronics

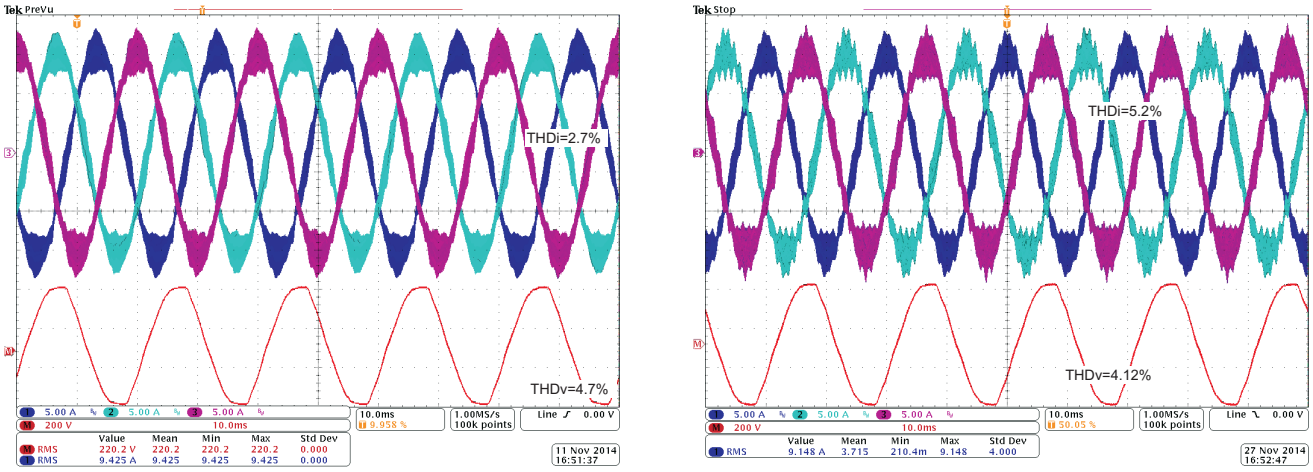

(a) GPCC (b) PR

Fig. 8. Experimental steady state three-phase output currents (above) along with one of the grid voltage waveforms (below). At the (left) GPCC with $\text{THD}_i = 2.7\%$ @$I = 13\,\text{A}_\text{p}$,$THD_v = 4.7\%$ and at (right) PR steady state with $\text{THD}_i = 5.2\%$@$I = 13\,\text{A}_\text{p}$, $THD_v = 4.12\%$.

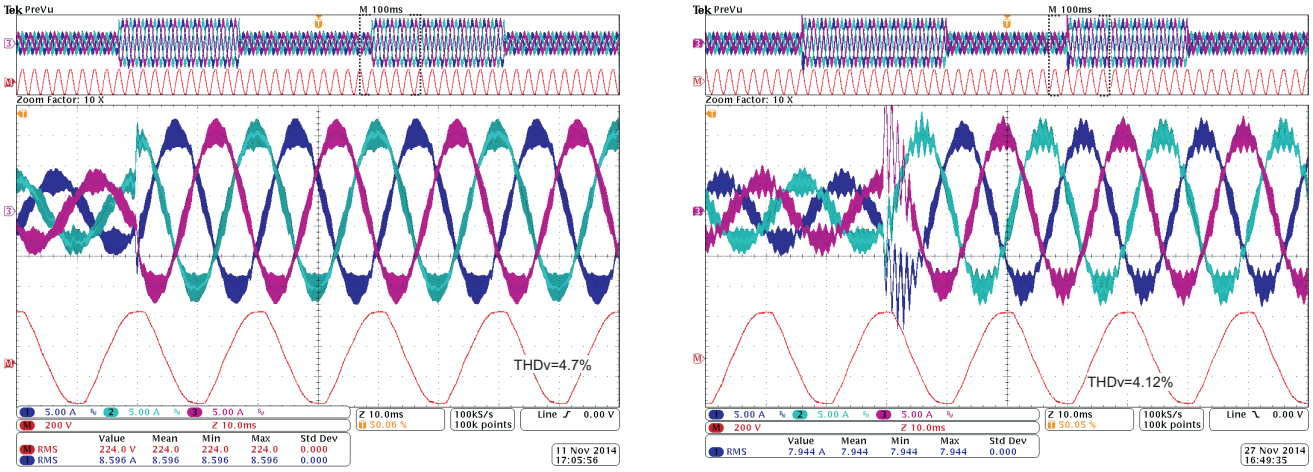

(a) GPC (b) PR

Fig. 9. Multiple amplitude reference step changes (top), a detail of the transition between $5A_p$ ($P_o = 4.33\,\text{kW}$) to $13A_p$ ($P_o = 10.83\,\text{kW}$) (middle) and one of the grid voltage waveforms (bottom). a) $THD_v = 4.7\%$. b) $THD_v = 4.12\%$

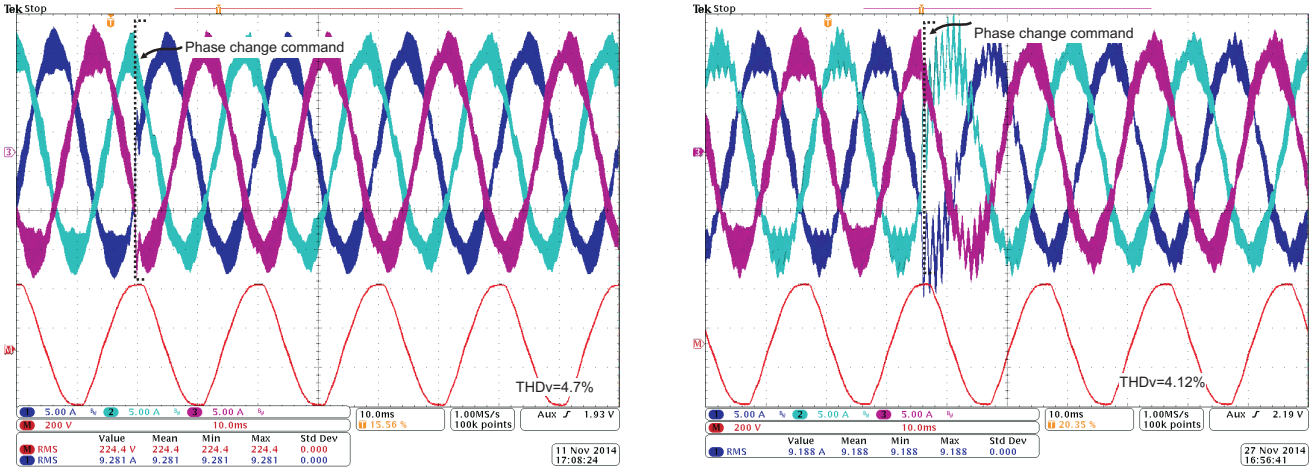

(a) GPCC (b) PR

Fig. 10. (a) GPCC and (b) PR three-phase grid-currents when a 30° phase change command is issued along with one of the grid voltage waveforms. a) $THD_v = 4.7\%$. b) $THD_v = 4.12\%$

This article has been accepted for publication in a future issue of this journal, but has not been fully edited. Content may change prior to final publication. Citation information: DOI 10.1109/TIE.2015.2508934, IEEE Transactions on Industrial Electronics

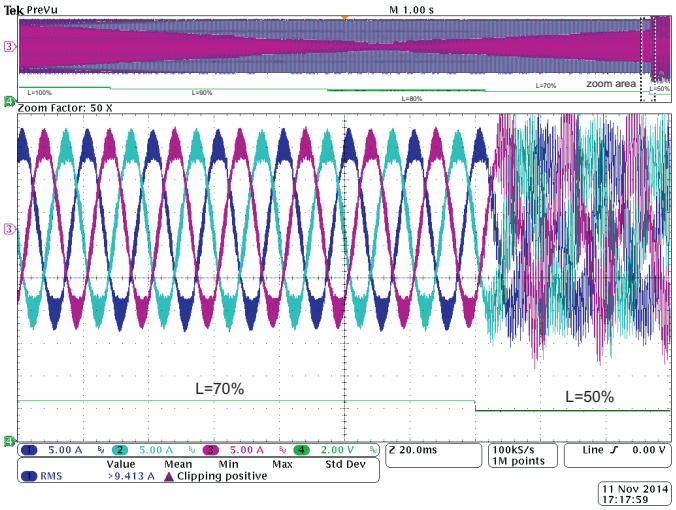

Fig. 11. GPCC three-phase output currents (top), a detail of the current waveforms when instability occurs (middle) and a trace of L as a percentage of the model inductance(bottom). Instability occurs when L decreases from 70% to 50%.

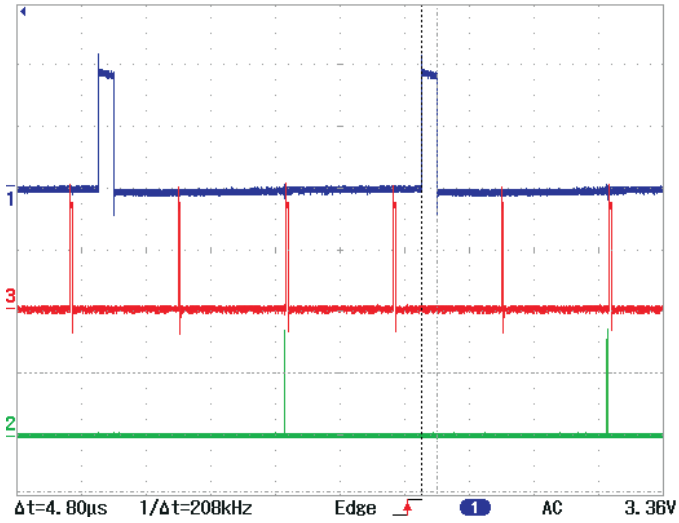

Fig. 12. Total GPCC computation time (three phases). Ch.1 pulse period equals the total computation time and Ch.2 pulses mark the PWM duty-cycle update instant. Ch.3 represent the sampling instants of the ADC. A LeCroy 324A oscilloscope was used to obtain the computational performance results.

C. Calculation time

An important feature of an industrial control system is a low computational burden, which implies lower hardware system requirements. Therefore, a simple experiment was made in order to determine the total time the controller spends in the control input calculation, and evaluate its performance. This is shown in the oscilloscope upper trace of Fig. 12, where a pulse of $4.80\,\mu$s represents the time window spent by the microprocessor to make control calculations for all three phases. The lower trace shows PWM update instants, which are equidistant in time, as expected. The middle trace depicts sampling instants of the ADC. As can be seen, three samples are required by the FIR filter, as previously explained in section V, and centered around the PWM update instant. The time interval of $8.0\,\mu$s between the last acquisition pulse and the rising edge of the calculation window is due to the acquisition time and digital filtering algorithm. Therefore, a $T_c = 12.80\,\mu$s total computation time is achieved with the proposed controller. Considering these results and in order to assess its performance a comparison with other control strategies is shown in Table III. These controllers were selected by considering same hardware platform as the proposed GPCC and explicit availability of both THD$_i$ and calculation time values.

TABLE III
CONTROLLER PERFORMANCE COMPARISON.

Control Strategy	$T_c[\mu s]$	THD$_i$
Lyapunov FCS-MPC [37]	6.8	5.27%
OSSDPC [38]	40	2.9%
PR+HC [39]	21	2.4%
PR [17]	17.5	1.5%

The uppermost part of the table contains two predictive control strategies, along with its corresponding performance indicators. Lyapunov FCS-MPC [37], does not meet current quality THD$_i$ standards, which is slightly over 5%. On the other hand, OSSDPC [38] has a THD$_i$ of 2.9% which is well within acceptable limits, but presents a longer computation time. The lowest part of the table contains another two control strategies based on standard grid-tie controllers. Both meet current quality standards, and the modified PR strategy [17] obtains the lowest THD$_i$ percentage, and less computational burden. By observing these results, it is evident that GPCC presents the lowest calculation time of $12.8\,\mu$s and also meets current quality standards with a THD$_i$ value of 2.7% which is a very good result, considering its low computational complexity.

VII. CONCLUSIONS

In this work a linear Generalized Predictive Current Control (GPCC) for DPGS inverters was introduced and a novel design procedure for the proposed controller was presented. This method allows a control system designer to set the desired control behavior, *a priori*. It was obtained by means of an analytical assessment of the λ controller parameter and its effect on bandwidth and robustness. This eases the controller design process, in comparison with standard MPC techniques, avoiding the trial an error tuning process characteristic of cost-function based strategies. The resulting controller achieves a fast response and at the same time, low current distortion, complying with current control requirements.

Experimental results show that GPCC meets quality standards and outperforms classical controllers, such as the PR control, both in steady-state and transient response. A steady state THD$_i$ value of 2.7% was obtained, in comparison with a 5.2% resultant of a suboptimal systematic PR design. This reflects the fact that the proposed controller is far from the 5% maximum allowable THD$_i$ values imposed by the standards, as opposed to the PR controller which is slightly off-limits. Also, system robustness criteria is experimentally proven and coherent with the design process. Finally, GPCC calculation time is $12.8\,\mu$s which is far less that other MPC strategies and also

smaller than the time required by a low THD_i PR controller formulation. Therefore, the proposed GPCC technique can be included as a practical controller in industrial grid-tie inverters, even without powerful hardware platforms, as opposed to other computationally demanding MPC strategies.

REFERENCES

[1] F. Blaabjerg, Z. Chen, and S. Kjaer, "Power electronics as efficient interface in dispersed power generation systems," *IEEE Trans. Power Electron.*, vol. 19, no. 5, pp. 1184–1194, Sept 2004.

[2] M. A. Herrán, , J. R. Fischer, S. A. González, M. G. Judewicz, and D. O. Carrica, "Adaptive dead-time compensation for grid-connected PWM inverters of single-stage PV systems," *IEEE Trans. Power Electron.*, vol. 28, no. 6, pp. 2816 –2825, Jun. 2013.

[3] F. Wu, F. Feng, L. Luo, J. Duan, and L. Sun, "Sampling period online adjusting-based hysteresis current control without band with constant switching frequency," *IEEE Trans. Ind. Electron.*, vol. 62, no. 1, pp. 270–277, Jan 2015.

[4] S.-W. Kang and K.-H. Kim, "Sliding mode harmonic compensation strategy for power quality improvement of a grid-connected inverter under distorted grid condition," *Power Electronics, IET*, vol. 8, no. 8, pp. 1461–1472, 2015.

[5] J. Rodriguez, J. Pontt, C. Silva, P. Correa, P. Lezana, P. Cortes, and U. Ammann, "Predictive current control of a voltage source inverter," *IEEE Trans. Ind. Electron.*, vol. 54, no. 1, pp. 495–503, Feb 2007.

[6] S. Kouro, P. Cortes, R. Vargas, U. Ammann, and J. Rodriguez, "Model predictive control - a simple and powerful method to control power converters," *IEEE Trans. Ind. Electron.*, vol. 56, no. 6, pp. 1826 –1838, Jun. 2009.

[7] J. Rodriguez, M. Kazmierkowski, J. Espinoza, P. Zanchetta, H. Abu-Rub, H. Young, and C. Rojas, "State of the art of finite control set model predictive control in power electronics," *IEEE Trans. Ind. Informat.*, vol. 9, no. 2, pp. 1003–1016, May 2013.

[8] M. G. Judewicz, J. R. Fischer, M. A. Herrán, S. A. González, and D. O. Carrica, "A robust model predictive control for grid-connected voltage-source inverters," *IEEE Lat. Am. Trans.*, vol. 11, no. 1, pp. 27–31, Apr. 2013.

[9] R. Ramirez, J. Espinoza, P. Melin, M. Reyes, E. Espinosa, C. Silva, and E. Maurelia, "Predictive controller for a three-phase/single-phase voltage source converter cell," *IEEE Trans. Ind. Informat.*, vol. 10, no. 3, pp. 1878–1889, Aug 2014.

[10] X. Zhang, Y. Wang, C. Yu, L. Guo, and R. Cao, "Hysteresis Model Predictive Control for High-Power Grid-Connected Inverters with Output LCL-Filter," *IEEE Trans. Ind. Electron.*, vol. PP, no. 99, pp. 1–1, 2015.

[11] P. Cortés, J. Rodríguez, D. Quevedo, and C. Silva, "Predictive current control strategy with imposed load current spectrum," *IEEE Trans. Power Electron.*, vol. 23, no. 2, pp. 612 –618, Mar. 2008.

[12] M. Judewicz, J. Fischer, N. Echeverria, S. A. González, and D. Carrica, "Filtro notch digital para la conformación del espectro en control predictivo basado en modelo," in *Biennial Congress of Argentina (ARGENCON), 2014 IEEE*, Jun. 2014, pp. 1–6.

[13] L. Tarisciotti, P. Zanchetta, A. Watson, S. Bifaretti, and J. Clare, "Modulated model predictive control for a seven-level cascaded h-bridge back-to-back converter," *IEEE Trans. Ind. Electron.*, vol. 61, no. 10, pp. 5375–5383, Oct 2014.

[14] M. Singh and A. Chandra, "Real-time implementation of anfis control for renewable interfacing inverter in 3p4w distribution network," *IEEE Trans. Ind. Electron.*, vol. 60, no. 1, pp. 121–128, Jan 2013.

[15] Y. Cheng, K. Chen, L. Bai, and J. Yang, "Improvement of the grid-connect current quality using novel proportional-integral controller for photovoltaic inverters," *Review of Scientific Instruments*, vol. 85, no. 2, pp. 025 110–025 110–8, Feb 2014.

[16] C. Busada, S. Gomez Jorge, and J. Solsona, "Full-State Feedback Equivalent Controller for Active Damping in LCL -Filtered Grid-Connected Inverters Using a Reduced Number of Sensors," *IEEE Trans. Ind. Electron.*, vol. 62, no. 10, pp. 5993–6002, Oct 2015.

[17] M. Castilla, J. Miret, A. Camacho, J. Matas, and L. de Vicuna, "Reduction of current harmonic distortion in three-phase grid-connected photovoltaic inverters via resonant current control," *IEEE Trans. Ind. Electron.*, vol. 60, no. 4, pp. 1464–1472, Apr. 2013.

[18] J. Kukkola and M. Hinkkanen, "Observer-based state-space current control for a three-phase grid-connected converter equipped with an LCL filter," *IEEE Trans. Ind. Applicat.*, vol. 50, no. 4, pp. 2700–2709, Jul. 2014.

[19] C. Bordons and C. Montero, "Basic Principles of MPC for Power Converters: Bridging the Gap Between Theory and Practice," *IEEE Ind. Electron. Mag.*, vol. 9, no. 3, pp. 31–43, Sep. 2015.

[20] K. Nishida, T. Ahmed, and M. Nakaoka, "Cost-effective deadbeat current control for wind-energy inverter application with lcl filter," *IEEE Trans. Ind. Applicat.*, vol. 50, no. 2, pp. 1185–1197, March 2014.

[21] J. R. Fischer, S. A. González, M. A. Herrán, M. G. Judewicz, and D. O. Carrica, "Calculation-delay tolerant predictive current controller for three-phase inverters," *IEEE Trans. Ind. Informat.*, vol. 10, no. 1, pp. 233–242, Feb. 2014.

[22] J. Mattingley, Y. Wang, and S. Boyd, "Receding horizon control," *IEEE Control Syst. Mag.*, vol. 31, no. 3, pp. 52–65, Jun. 2011.

[23] S. Mariethoz and M. Morari, "Explicit model-predictive control of a PWM inverter with an LCL filter," *IEEE Trans. Ind. Electron.*, vol. 56, no. 2, pp. 389–399, Feb 2009.

[24] D. Clarke, C. Mohtadi, and P. Tuffs, "Generalized Predictive Control - Part I. The basic algorithm," *Automatica*, vol. 23, no. 2, pp. 137–148, 1987.

[25] H. Demircioglu and E. Karasu, "Generalized predictive control. a practical application and comparison of discrete- and continuous-time versions," *IEEE Control Syst. Mag.*, vol. 20, no. 5, pp. 36–47, 2000.

[26] L. Zhang, R. Norman, and W. Shepherd, "Long-range predictive control of current regulated PWM for induction motor drives using the synchronous reference frame," *IEEE Trans. Contr. Syst. Technol.*, vol. 5, no. 1, pp. 119–126, Jan 1997.

[27] K.-S. Low, "A digital control technique for a single-phase PWM inverter," *IEEE Trans. Ind. Electron.*, vol. 45, no. 4, pp. 672–674, Aug. 1998.

[28] R. Kennel, A. Linder, and M. Linke, "Generalized predictive control (gpc)-ready for use in drive applications?" in *Proc. PESC Power Electronics Specialists Conference 2001 IEEE 32nd Annual*, vol. 4, 2001, pp. 1839–1844 vol. 4.

[29] T. Allaoui, M. Denaï, and M. Bouhamida, "Decoupling multivariable GPC control of UPFC-based power flow compensation," in *10th International Conference EPE-PEMC*, 2002.

[30] S. Vazquez, C. Montero, C. Bordons, and L. Franquelo, "Design and experimental validation of a model predictive control strategy for a VSI with long prediction horizon," in *Industrial Electronics Society, IECON 2013 - 39th Annual Conference of the IEEE*, Nov 2013, pp. 5788–5793.

[31] F. Blaabjerg, R. Teodorescu, M. Liserre, and A. Timbus, "Overview of control and grid synchronization for distributed power generation systems," *IEEE Trans. Ind. Electron.*, vol. 53, no. 5, pp. 1398 –1409, Oct. 2006.

[32] D. Clarke, *Advances in model-based predictive control*. Oxford ; New York : Oxford University Press, 1994.

[33] J. M. Maciejowski, *Predictive Control: With Constraints*, ser. Pearson Education. Prentice Hall, 2002.

[34] I. Carugati, S. Maestri, P. Donato, D. Carrica, and M. Benedetti, "Variable sampling period filter PLL for distorted three-phase systems," *IEEE Trans. Power Electron.*, vol. 27, no. 1, pp. 321–330, Jan. 2012.

[35] N. Zhang, H. Tang, and C. Yao, "A systematic method for designing a PR controller and active damping of the LCL filter for single-phase grid-connected PV inverters," *Energies*, vol. 7, no. 6, pp. 3934–3954, 2014.

[36] E.ON Netz GmbH, *Grid Connections Regulations to High and Extra High Voltage*, E.ON Netz GmbH Std., Apr. 2006.

[37] S. Kwak, S.-J. Yoo, and J. Park, "Finite control set predictive control based on Lyapunov function for three-phase voltage source inverters," *Power Electronics, IET*, vol. 7, no. 11, pp. 2726–2732, Nov. 2014.

[38] S. Vazquez, A. Marquez, R. Aguilera, D. Quevedo, J. Leon, and L. Franquelo, "Predictive Optimal Switching Sequence Direct Power Control for Grid-Connected Power Converters," *IEEE Ind. Electron. Mag.*, vol. 62, no. 4, pp. 2010–2020, Apr. 2015.

[39] Y. Jia, J. Zhao, and X. Fu, "Direct grid current control of LCL-filtered grid-connected inverter mitigating grid voltage disturbance," *IEEE Trans. Power Electron.*, vol. 29, no. 3, pp. 1532–1541, Mar. 2014.

Marcos G. Judewicz (S'11) received the Ing. degree in electronics engineering from the Universidad Nacional de Mar del Plata, Mar del Plata, Argentina, in 2011, where he is currently working toward the Ph.D. degree. His current research interests include industrial electronics, power converters, and model predictive control. Mr. Judewicz is a Member of the IEEE Industrial Electronics Society.

Sergio Alejandro González (M'01) was born in Mar del Plata, Argentina, in 1972. He received the Ing. and Dr. Ing. degrees in electronic engineering from the Universidad Nacional de Mar del Plata (UNMdP), Mar del Plata, in 1999 and 2006, respectively. Since 1999, he has been an Assistant Professor of control systems in the School of Engineering, UNMdP. He is currently a researcher at the ICYTE (Instituto de Investigaciones Científicas y Tecnológicas en Electrónica), UNMdP, and a member of the National Scientific and Technical Research Council (CONICET), Buenos Aires, Argentina. His scientific interests include hardware design, digital signal processing, digital control techniques for electrical power systems and integration of distributed energy systems. Dr. González is a member of the IEEE Industrial Electronics Society.

Noelia I. Echeverria received the Ing. degree in electronics engineering from the Universidad Nacional de Mar del Plata, Mar del Plata, Argentina, in 2012, where she is currently working toward the Ph.D. degree. Her current research interests include industrial electronics, adaptive control systems, and model identification.

Jonatan Roberto Fischer (S'09) received the Ing. degree in electronics engineering from the Universidad Nacional de Mar del Plata (UNMdP), Mar del Plata, Argentina, in 2008 and in 2013 he received the Dr. Ing. degree. His research interests are power electronics, control systems, and digital signal processing. Dr. Fischer is a member of the IEEE Industrial Electronics Society.

Daniel O. Carrica (S'85-M'95-SM'08) received the B.S. degree in engineering from the Universidad Nacional de Mar del Plata (UNMdP), Mar del Plata, Argentina, in 1984, M.Sc. degree in electronics from the Universidad Politécnica de Madrid, Madrid, Spain, in 1992 and the Ph.D degree in 2006 from the UNMdP.

In 1984, he joined the Department of Electronics, UNMdP where he is currently a Full Professor. From 1990 to 1992, he was an Associate Scientist at the European Organization for Nuclear Research, Geneva, Switzerland. He is currently Head of ICYTE (Instituto de Investigaciones Científicas y Tecnológicas en Electrónica), Facultad de Ingeniería, Universidad Nacional de Mar del Plata.